




Facile Synthesis of Boron-Doped Reduced Electrochemical Graphene Oxide for Sodium Ion Battery Anode

YUBAI ZHANG,¹ JIADONG QIN,¹ MUNKHBAYAR BATMUNKH,¹
and YU LIN ZHONG ^{1,2}

1.—Centre for Catalysis and Clean Environment, School of Environment and Science, Gold Coast Campus, Griffith University, Gold Coast, Queensland 4222, Australia. 2.—e-mail: y.zhong@griffith.edu.au

In this work, we present a facile yet effective method to prepare boron-doped, highly reduced electrochemical graphene oxide (B-rEGO) using electrochemical oxidation coupled with high-temperature thermal reduction. We first fabricated EGO from natural graphite powder in different concentrations of sulfuric acid electrolytes in a packed-bed reactor and found that the 12 M acid could produce EGO with the highest level of oxidation. To introduce heteroatom doping (non-metallic boron), sufficient boric acid was added to the sulfuric acid electrolyte for electrochemical reactions whereby the boron-doped graphene precursor could be formed, namely tetraborate anion intercalated EGO compounds, and it could transform into B-rEGO by annealing at 900 °C for 3 h under Ar gas. We found that the B-rEGO was highly defective as well as effectively deoxygenated and contained 0.21 at.% of boron. The as-prepared B-rEGO is used as an active material in sodium ion battery anodes, delivering a good capacity of 129.59 mAh g⁻¹ at the current density of 100 mA g⁻¹ and long-term cyclic stability which could retain 100.20 mA g⁻¹ after 800 cycles at 500 mA g⁻¹.

INTRODUCTION

Sodium ion batteries (SIBs) are considered a promising, cheaper alternative to lithium-ion batteries (LIBs),^{1–4} but the commercial graphite-based anodes, which are commonly employed in LIBs, are not suitable in SIBs because of the insufficient interlayer space for the larger sodium (Na) ions with a diameter of 2.04 Å (Li ion is only 1.52 Å in size).⁵ To address this issue, activating graphitic anodes for high Na storage capability has attracted significant research interest over the past several years. Graphene, a two-dimensional (2D) carbon allotrope, can provide short paths for charge transportation and ultra-large surface areas to accommodate metal ions in rechargeable batteries, making it a potential reliable platform for sodium storage.^{6–13} Nevertheless, both experimental and theoretical calculations have indicated that atomically thin graphene is energetically unfavorable for Na ion adsorption

unless high defect density is introduced to graphene.¹⁴ With this motivation, a variety of graphene-derived materials, with a major focus on oxidation and elemental doping of graphene,^{15,16} for high performance anodes of SIBs have been reported over the past decade.^{14,17–19}

The oxidation of graphene can cause significant changes in electronic properties and reactivity with Na ion.^{20–22} The role of oxygen functional groups for Na ion intercalation in graphene oxide (GO) has been studied using density functional theory (DFT), and it was found that epoxide groups attached on graphene oxide (GO) can make a great contribution to Na storage capacity as well as efficient charge transport.²³ Besides, in the process of oxidation the corrosion of the carbon network usually occurs, which creates many vacancy defects in GO products. It is noteworthy that the adsorption energy of Na ions on the vacancy of graphene (–2.46 eV) is about 3.4 times higher than that on the pristine graphene (–0.71 eV), leading to enhanced sodium storage capacity on defective graphene 10–30 times higher than that of pristine graphene.²⁴ Mild reduction of

GO is used to control the density of oxygen-containing groups to improve charge transportation because partial removal of oxygen from GO can help reduce the steric impediment of oxygen groups to Na ion intercalation and improve the electric conductivity.¹⁷

As to the elemental doping method, Dobrota et al. have investigated the influence of substitutional boron elemental doping on the adsorption energy of graphene with Na ion, and they suggested that boron-doped GO prepared by controlled oxidation delivered enhanced adsorption of Na ions.²¹ To prepare boron-doped graphene, various techniques have been proposed, such as vapor phase deposition²⁵ and post-synthesis treatment where boron doping is introduced to preformed grapheme.^{26,27} The latter is widely adopted to fabricate boron-doped graphene for energy storage applications, such as lithium-ion batteries and supercapacitors. Boric acid powders are commonly used as boron dopants to mix homogeneously with GO. High temperature annealing (900–1200 °C) is applied to the mixture of boron dopants and GO under inert atmosphere to realize simultaneous boron doping and reduction of GO.^{28–30} Niaura et al. studied the reduction of GO in the melt of boric acid in 2018; they found that the threefold coordinated boron atom can serve as a scavenger of oxygen during the annealing process, which leads to the formation of a less disordered structure and increases the concentration of point defects on the basal planes of grapheme.³¹ To fabricate GO, natural graphite (NG), which is commonly used as a starting material, is oxidized chemically or electrochemically, followed by exfoliation.^{21,32–35} The electrochemical method is superior to conventional chemical oxidation in terms of a more controllable and greener manufacturing process. The oxidation of graphite is driven by the intercalation of ions and molecules into graphite interlayers under an external bias in a suitable electrolyte solution.^{36,37}

In this work, we first investigated the optimum concentration of sulfuric acid electrolyte (among 7 M, 12 M and 16 M) for the synthesis of EGO and determined that the use of 12 M acid could result in the product with highest level of oxidation, leading to an optimum sodium storage capacity. To study the contribution of boron doping to the EGO-based SIBs' performance, we dissolved boric acid in sulfuric acid as the mixed electrolytes for the electrochemical fabrication of EGO. The dissolved boric acid in water can form tetraborate anions which can intercalate into graphite under galvanostatic charging and serve as boron dopants during the subsequent thermal post-processing.^{28,38,39} The high-temperature annealing (900 °C for 3 h under Ar atmosphere) was operated on the precursor (tetraborate anion intercalated EGO compounds) to produce highly reduced boron-doped graphene (B-rEGO). The elemental analysis showed that 0.21 at.% boron was doped to graphene after annealing, and as fabricated

B-rEGO exhibited notably improved battery performance compared to the undoped counterpart when applied to the SIB anodes.

EXPERIMENTAL SECTION

Synthesis of EGO and rEGO

To synthesize EGO, we used the apparatus and method as described comprehensively in our previous work.¹⁹ The electrochemical glass tubular reactor is shown in Fig. 1a. In a typical experiment, 160 mg of natural graphite (Sigma Aldrich, Product No. 332461) was poured into the reactor bottom to form a bed, and three layers of glass fiber membranes were used as the separator to sit on the top of the bed. Then, the membranes along with the bed were pressed by a weight of 0.5 kg from the top onto the boron-doped diamond (BDD), which served as the working electrode. A coiled Pt wire takes the role of counter electrode; 3.6 mL of 7 M to 16 M sulfuric acid electrolyte (diluted from 98% sulfuric acid supplied from ChemSupply Australia) was pipetted individually into the glass tubular reactor as electrolyte. The BDD plate and Pt wire were connected to a potentiostat (Gamry interface 1000, Warminster, PA), which provides constant positive current of 16 mA to BDD. Once the electrochemical reaction finished, EGO products were decanted from the reactor and washed with plenty of DI water by filtration to remove the sulfuric acid, and then the EGO was decanted into 125 mL DI water and sonicated for 10 min before filtration to obtain the final products. The washed EGO products were dried in a freeze dryer for 2–3 days. For the fabrication of the tetraborate anion intercalated EGO, saturated boric acid (0.92 M) was added into 12 M sulfuric acid as the electrolyte, and after reaction no wash procedure was needed before annealing to avoid cleaning out the intercalated tetraborate anions. In terms of the reduction procedure, the EGO and tetraborate anion intercalated EGO compound were annealed in a tube furnace at 900 °C holding for 3 h under Ar atmosphere. For washing the B-rEGO sample, the annealed products were decanted into DI water and stirred for 3 h at 60–70 °C to dissolve any residual boric acid. Then, the B-rEGO dispersion was rinsed with plenty of water by filtration. The washed B-rEGO was frozen before being put into a freeze dryer for 2–3 days to obtain the final products.

Electrochemical Test

EGO (7 M, 12 M and 16 M activated EGO) and reduced products (rEGO and B-rEGO) were individually blended with conductive additive carbon black and PVDF binder in a mass ratio of 7:2:1 in *N*-methyl-2-pyrrolidone (NMP) solvent to form a uniform slurry before coating onto carbon-coated copper foil by a doctor blade with a thickness of 400 μm. The mass loading density of active material was 0.5

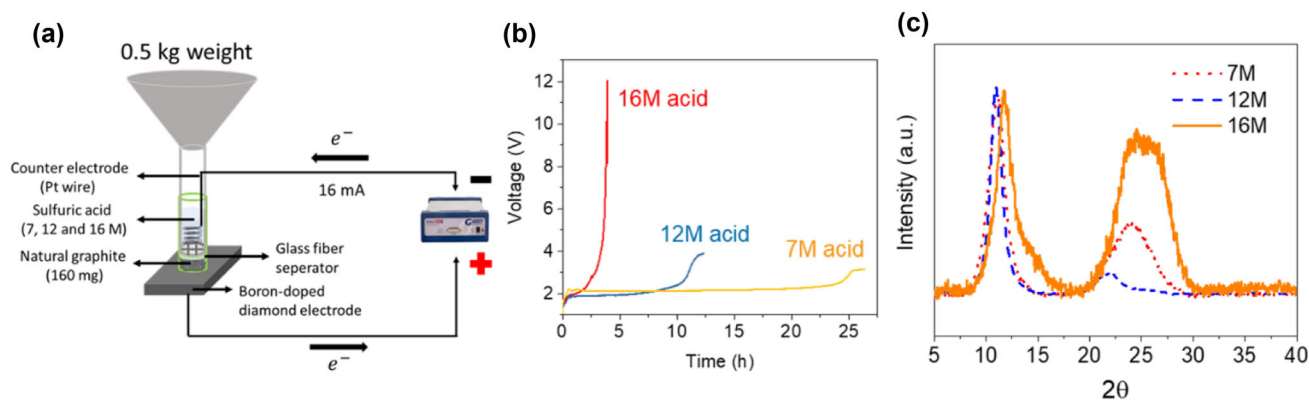


Fig. 1. Electrochemical synthesis of EGO in a small glass tubular packed-bed reactor and the material characterizations. (a) Schematic illustration of the electrochemical reactor. (b) The galvanostatic electrochemical reaction curve of 160 mg NG packed bed in three concentrations of sulfuric acid. (c) XRD patterns of EGO products from 160 mg NG in varied concentrations of sulfuric acid (7 M, 12 M and 16 M).

mg cm⁻²; 1 M NaClO₄ in propylene carbonate (PC) and 5 wt.% fluoroethylene carbonate (FEC) were used as SIB electrolyte. Glass fiber was used as separator in between the sodium metal anode and the tested cathode. The 2032 coin cells were assembled in an Ar-filled glove box. The battery tests were performed on a Neware battery testing system with voltage window of 0.02 V to 3 V in galvanostatic charge-discharge mode.

Material Characterizations

For x-ray powder diffraction (XRD), x-ray photoelectron spectroscopy (XPS), electrical conductivity and Raman spectroscopy measurements, EGO samples were formed into a free-standing membrane by vacuum filtration. XRD patterns were measured on a Bruker D8 Advance diffractometer. XPS was performed on a Kratos Axis ULTRA incorporating a monochromatized Al K_α x-ray source, and the collected data were analyzed using Casa XPS software with a Shirley background subtraction. The sheet resistance of EGO membranes was measured using a Jandel RM3000 four-point probe system with a linear arrayed head with probe spacing of 1 mm. The electrical conductivity (S m⁻¹) of the EGO membrane was calculated based on the film thickness and resistance (Ω per square). Raman spectroscopy was performed on a Renishaw inVia Raman microscope equipped with a 532-nm laser. Renishaw Wire 5.0 software was used for background subtraction and peak fitting. Transmission electron microscopy (TEM) images were captured using a JEOL JEM-2100F with an accelerating voltage of 200 kV. To prepare TEM samples, the powder samples were sonicated in ethanol for 5 min before drop casting on a holey carbon film gold grid and then dried in air.

RESULTS AND DISCUSSIONS

Optimizing Sulfuric Acid Concentration for GO Preparation

As illustrated in Fig. 1a, different concentrations of sulfuric acid (7 M, 12 M and 16 M) and 160 mg NG were used in electrochemical production of EGO. Upon applying a constant positive current of 16 mA, three typical regions were exhibited in the potential versus time curves, as shown in Fig. 1b. A short induction region was followed by a long potential stage of oxidation, and then a sharp increase of potential ended with a constant slope. The short induction was ascribed to the formation of GIC, while the sharp increasing potential was because of oxidation of water replacing the oxidation of the packed bed. The diluted acid would prolong the packed bed oxidation time, as has been stated previously.³⁶ XRD patterns of final EGO products are displayed in Fig. 1c; 160 mg NG bed could be oxidized at all three acid concentrations, as is evident by the strong GO peak between 10° and 15°. In addition, a broad peak in the range of 24° to 25° remained in the EGO samples prepared at 16 and 7 M acid, which is attributed to the less oxidized parts.

The final mass yield of EGO activated at 7 M, 12 M and 16 M acids is depicted in Fig. 2a. It is obvious that EGO produced from 12 M acid electrolyte has the highest mass gain, reaching 172% relative to the initial loading of NG. The XPS survey scan in Fig. 2b demonstrates that the EGO synthesized at 12 M acid had relatively lower C/O ratio (3.22) compared to that for 16 M (3.95) and 7 M (3.60). It is noteworthy that, compared to the 16 M acid-activated EGO, the 7 M acid-activated one has smaller mass gain but lower C/O ratio (or higher content of

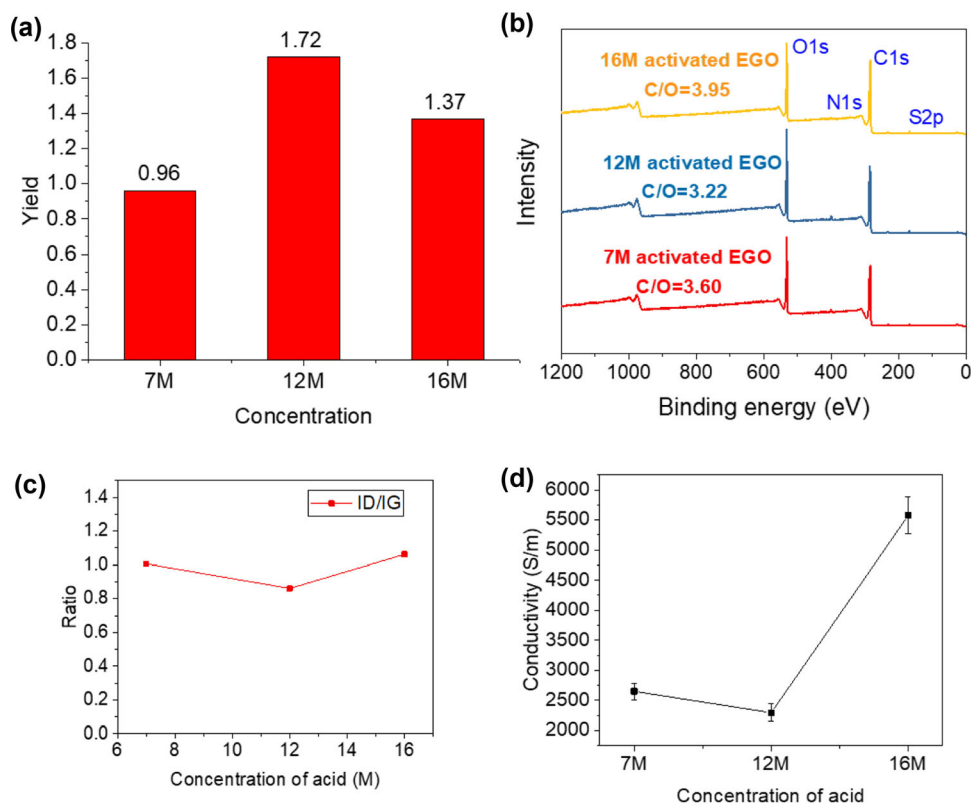


Fig. 2. Comparison of chemical and physical properties of EGO reacted in different concentrations of sulfuric acid. (a) Yield of 160 mg NG loading after reaction in 7 M to 16 M sulfuric acid (dried EGO product versus starting NG). (b) XPS survey spectra of 7 M acid-activated EGO (consisting of approximately 21.39 at% oxygen and 77.05 at% carbon), 12 M acid-activated EGO (23.06 at% oxygen and 74.30 at% carbon) and 16 M acid-activated EGO (19.94 at% oxygen and 78.78 at% carbon), and the minor sulfur impurity has been explained in our previous work,^{18,53} while the nitrogen may be associated with the glue substrate. (The atomic content table was in Table S1.) (c) Intensity ratios of I_D/I_G based on the fitting results in Figure S1. (d) Comparison of electrical conductivity of EGO membranes.

oxygen). This phenomenon is related to the over-oxidation of carbon, which results in CO_2 gas when more water molecules are present in the 7 M acid electrolyte. The oxidative species derived from water can initiate the carbon removal reactions, leaving defects in the final product.^{40–42} To characterize the structure of EGO, Raman spectra were deconvoluted into three bands (D, D' and G band) following the fitting method described by Clarumunt et al., as shown in Figure S1.^{43,44} The values of I_D/I_G are measured and summarized in Fig. 2c. According to the previous study,^{45–49} when incremental oxygen is introduced to pristine graphene, I_D/I_G increases with the defect density at the initial stage. Upon climbing to a critical defect concentration, however, I_D/I_G begins to decrease with defect density. In our experiment, the EGO prepared at 12 M acid is expected to contain the highest defect density due to its lowest I_D/I_G among the three samples. Also, for the 12 M acid-activated EGO, it has less interband area ($1500\text{--}1550\text{ cm}^{-1}$) between the D and G bands (Figure S2), which is associated with an additional component D'' band, than the other samples. Since the D'' band is activated by the presence of amorphous phases in carbon materials,^{50–52} it can be suggested that the 12 M acid-

activated EGO is less disordered and has greater crystallinity. In terms of electrical conductivity (Fig. 2d), the 16 M acid-activated EGO shows the highest conductivity of $5577.6\text{ S m}^{-1} \pm 309.3\text{ S m}^{-1}$, followed by the 7 M activated ($2648.6\text{ S m}^{-1} \pm 140.45\text{ S m}^{-1}$) and the 12 M activated ($2294.7\text{ S m}^{-1} \pm 144.4\text{ S m}^{-1}$).

The oxygen-containing functional groups of graphene nanosheets play critical roles in Na ion adsorption, which has been well documented.^{21,23,54} The deconvolution of x-ray photoelectron spectroscopy (XPS) C1s spectra of EGO (Fig. 3a, b and c) reveals that the 12 M acid-activated EGO has the highest content of epoxide and hydroxyl groups (43.52%), the lowest proportion of carboxylic groups (1.75%) and the lowest percentage of sp^2 carbon (51.10%). After being fitted into a half-cell SIB, the three EGO samples prepared at different acid concentrations delivered divergent capacities. The galvanostatic discharge/charge profiles of the three anodes at a high current density of 500 mA g^{-1} are shown in Fig. 3d. The 12 M acid-activated EGO could provide the highest Na ion storage capability compared with the other two samples, with a reversible charge capacity of 71.66 mAh g^{-1} . The discharge curve exhibits a sloping region from 3 V to

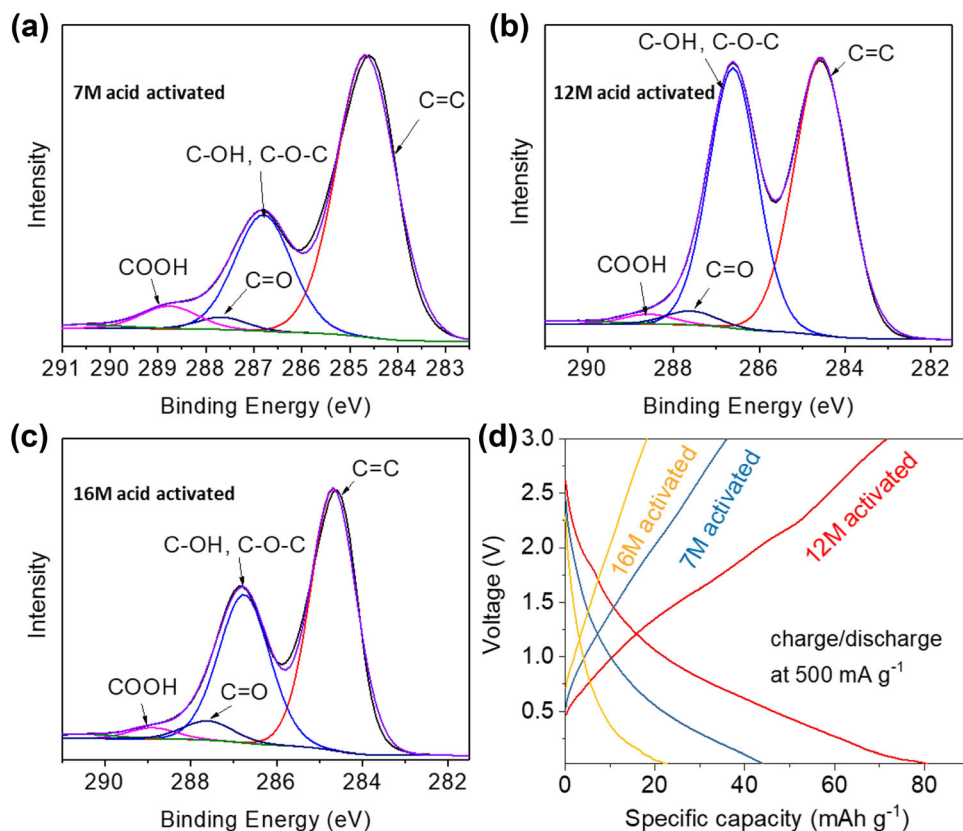


Fig. 3. Quantitative analysis of functional oxygen groups and electrochemical characterization of EGO products. (a)–(c) High-resolution C1s spectra of EGO activated in 7 M to 16 M acid, which are fitted into four components.⁵⁷ The deconvolution results are summarized in Table SII. (d) Galvanostatic charge/discharge profiles of 7 M to 12 M acid-activated EGO-based anodes at current density of 500 mA g⁻¹.

0.2 V and an inclined stage below 0.2 V, which is ascribed to Na ion adsorption on oxygen groups and/or defects and intercalation between the expanded GO layers, respectively.^{20,34,55,56} Therefore, the EGO prepared at 12 M sulfuric acid was further explored by thermal reduction, and the EGO mentioned below represents the 12 M sulfuric acid-activated EGO.

Fabrication of Highly Reduced GO

Highly reduced EGO was prepared to compare with unannealed EGO in terms of their Na ion storage capability. In the electrochemical reaction, saturated boric acid was added in the 12 M sulfuric acid electrolyte, which can provide tetraborate anions to intercalate into graphite layers and combine with the surface oxygen functional groups during exfoliation process.^{39,58} As depicted in Fig. 4a, the charging curves (voltage vs. time) under constant current of 16 mA show a similar trend, both of which are composed of three regions, as described above. However, the overall voltage in the electrolyte containing boric acid is higher than that in pure sulfuric acid, which should be ascribed to a thermodynamic interdiction of boric acid co-intercalation into graphite matrix with sulfuric acid.³⁹ After the electrochemical oxidation of NG, high temperature

reduction (900 °C for 3 h under Ar atmosphere) was operated on the two samples to study the effect of boric acid addition in electrolyte on the properties of reduced EGO products. Raman spectroscopy was used to characterize the original and reduced EGO. The D and G bands of graphene are located at around 1350 cm⁻¹ and 1575 cm⁻¹.^{57,59} After oxidation, the G band would be shifted to the right and broaden, while the D band would slightly shift to the left and become sharper because of the destruction of the *sp*² network and formation of defects associated with oxygen functional groups.⁶⁰ As labeled in Fig. 4b, the position of G band for EGO produced in the mixture of saturated boric acid and 12 M sulfuric acid (denoted as H₃BO₃-EGO) is shifted to higher wavenumber relative to EGO produced in pure sulfuric acid, indicating a more defective *sp*² network and addition of surface functional groups. The high temperature annealed products from EGO and H₃BO₃-EGO are marked as rEGO and B-rEGO. The D and G bands of rEGO were shifted back to 1349 cm⁻¹ and 1585 cm⁻¹, while the B-rEGOs were recovered to 1358 cm⁻¹ and 1585 cm⁻¹, indicating a successful reduction process. The intensity ratio of *I*_D/*I*_G of EGO and H₃BO₃-EGO was calculated to be about 0.86 and 0.72, while the intensity ratio of *I*_D/*I*_G of rEGO and B-rEGO increased to be 1.32 and 1.33, which suggests the successful removal of oxygen moieties and

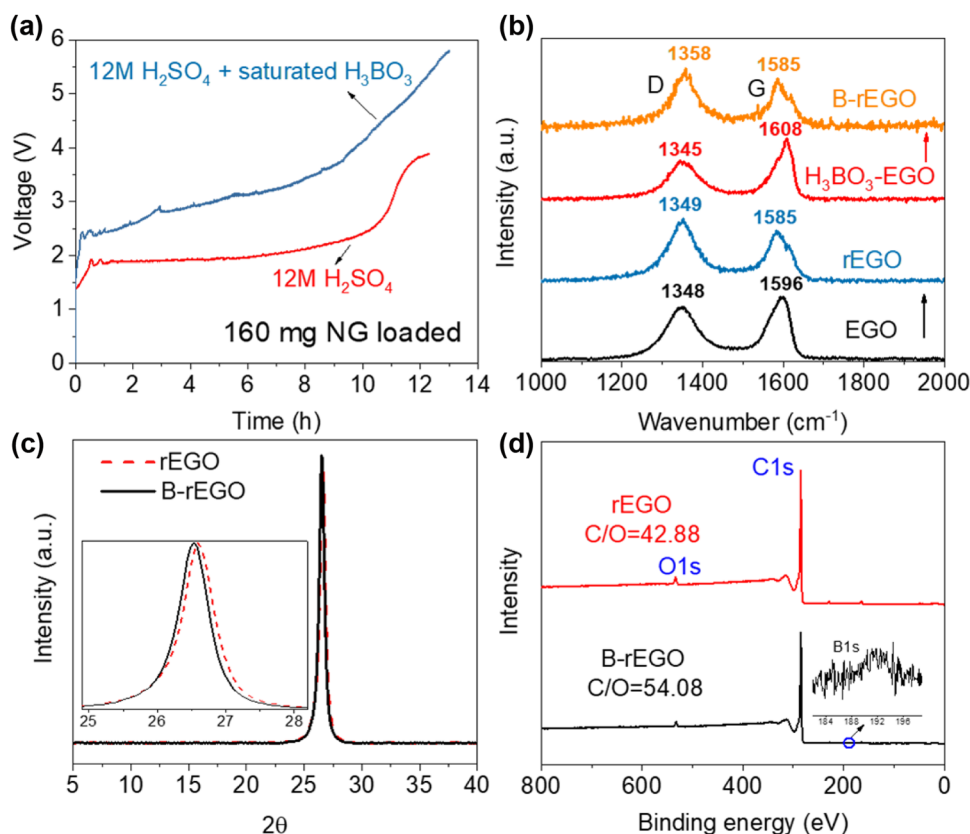


Fig. 4. Electrochemical synthesis of EGO with and without boric acid in electrolyte and the material characterizations. (a) The galvanostatic charging curves of electrochemical reaction in pure 12 M sulfuric acid and 12 M sulfuric acid with saturated boric acid addition. (b) Raman spectra of EGO synthesized in pure 12 M sulfuric acid and its reductants after annealing namely rEGO and EGO synthesized in 12 M sulfuric acid with saturated boric acid addition and its reductants after annealing namely B-rEGO. (c) XRD patterns of rEGO and B-rEGO. The inset is the magnified region of graphitic peaks for the two samples. (d) XPS survey spectra of rEGO and B-rEGO.

restoration of the sp^2 network after annealing.^{57,59,61} (The Raman spectra were deconvoluted into D, D' and G bands and exhibited in Figure S3.) The weaker D' peak of B-rEGO compared to rEGO suggested better crystallinity of the B-rEGO. The XRD patterns of rEGO and B-rEGO in Fig. 4c solely show a graphitic peak at 25.5° – 27.5° , which confirms that GO was fully converted to reduced GO (rGO). The interlayer spacing of B-rEGO was slightly larger than the rEGO and has greater crystallinity, as indicated by the smaller FWHZ of B-rEGO (0.524) compared to rEGO (0.542). XPS survey scans in Fig. 4d reveal that rEGO and B-rEGO have very high C/O ratios of 42.88 and 54.08, and a weak B1s peak at 192.2 eV in the B-rEGO sample indicates a tiny amount of boron (0.21 at.%), which has been doped in the final products. Compared with chemically made GO, electrochemically made GO shows higher thermal lability of oxygen groups,^{8,62,63} which accounts for the high C/O ratio in the rEGO and B-rEGO. The elemental proportions in Table SIII and the deconvolution of XPS C1s spectra in Figure S4 revealed in detail the proportion of oxygen groups in EGO, and H_3BO_3 -EGO was hugely reduced. The B-rEGO contains even fewer oxygen functional groups than

rEGO, because during annealing the intercalated tetraborate anion attached to C–O–C in H_3BO_3 -EGO can assist in creating functional group-free vacancy sites instead of formation of C=O group at the vacancy site, which can facilitate the fast ion transport in electrode material.^{8,31,62,63}

TEM and selected area electron diffraction (SAED) were used to uncover the lattice structure of rGO. During the thermal reduction process, the layered structure of GO would be distorted and reorganized.^{64–66} Figure 5a and b are the TEM images of rEGO and B-rEGO under low magnification, respectively; it can be clearly seen that the rEGO has a rough surface while the B-rEGO is flatter and smoother, indicating the B-rEGO has a more long-range-ordered layered structure. As shown in Fig. 5c and d, the high-resolution TEM (HRTEM) images show that the lattice structure of the edge of B-rEGO is more aligned and of higher crystallinity compared to rEGO and confirm the nanosheets in rEGO and B-rEGO both containing multi-layers. The insets in Fig. 5c and d are the corresponding SAED patterns of rEGO and B-rEGO. The pattern of rEGO is more diffused than B-rEGO suggesting a more amorphous structure of rEGO.

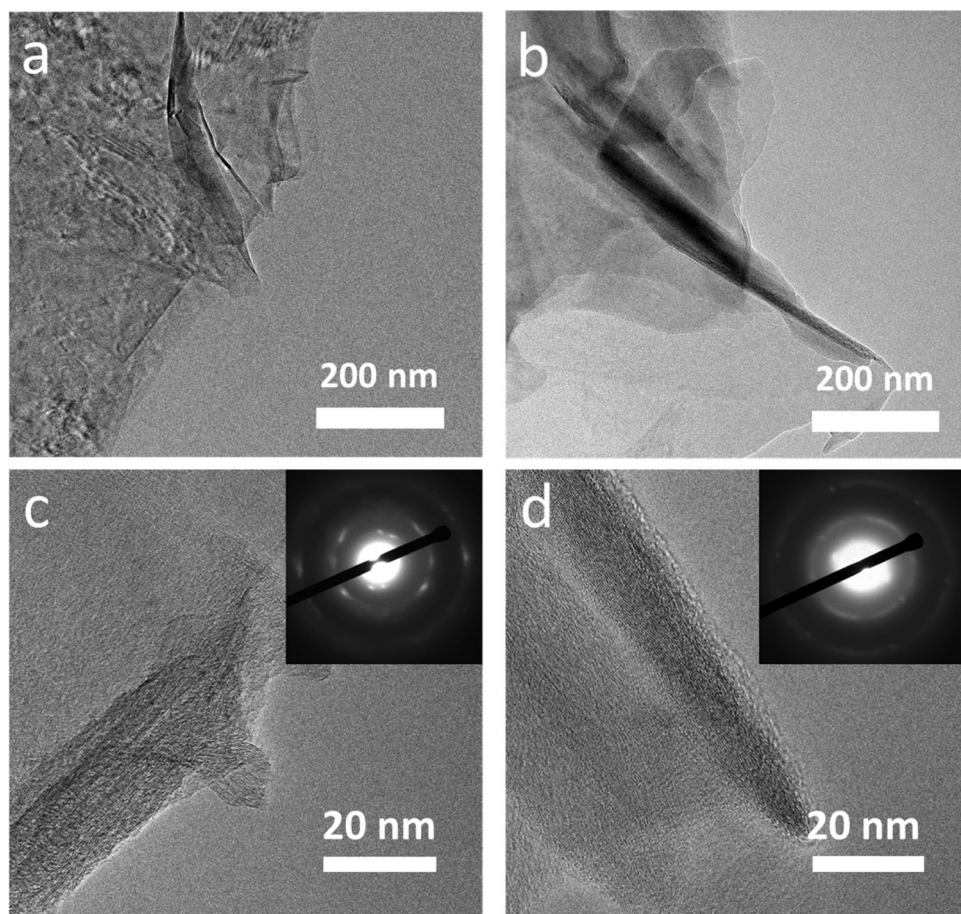


Fig. 5. TEM characterization of rEGO and B-rEGO samples. The TEM images of (a) rEGO and (b) B-rEGO under low magnification. HRTEM images taken on the edge area of (c) rEGO and (d) B-rEGO flake with inserted SAED patterns of the corresponding area.

SIBs Performance

The EGO and H_3BO_3 -EGO samples in their unreduced and reduced forms were used as the active materials in SIB anodes, respectively, and then were tested by galvanostatic charge and discharge. As shown in Fig. 6a, the capacity of B-rEGO-based anode shows higher charge capacity of $121.89 \text{ mAh g}^{-1}$ at current density of 100 mA g^{-1} than the other samples. Besides, compared with unannealed EGO and H_3BO_3 -EGO-based anodes, there is a more obvious voltage plateau in the charge curve of rEGO and B-rEGO anodes at the low voltage region, which could be envisaged to the sodium adsorption on the defective sites on graphene.³⁴ As illustrated in Fig. 6b, the charge/discharge profiles of B-rEGO-based anodes at varied current densities show sloping curves and relatively small voltage hysteresis between charge and discharge curves at the low voltage region (0–0.3V) under current density of 100 mA g^{-1} and 200 mA g^{-1} . The rate performance under various current densities is presented in Fig. 6c. The B-rEGO-based anode delivered the highest charge capacity compared with the other two samples, reaching an average charge capacity of 129.59 mA g^{-1} , 105.80

mA g^{-1} , 75.37 mA g^{-1} , 56.34 mA g^{-1} , 40.23 mA g^{-1} , 24.17 mA g^{-1} and mAh g^{-1} at current density of 100 mA g^{-1} , 200 mA g^{-1} , 500 mA g^{-1} , 1000 mA g^{-1} , 2000 mA g^{-1} and 5000 mA g^{-1} , respectively. When the current was reduced back to 100 mA g^{-1} , the average charge capacity of B-rEGO could recover to $121.62 \text{ mAh g}^{-1}$. The outstanding cyclic stability performance of the B-rEGO electrode is shown in Fig. 6d. The B-rEGO-based SIB presents an activation process where the charge capacity shows a slow increase during the 800 cycles and eventually attains a capacity of 100.20 mA g^{-1} , while obvious capacity decay can be found in the unannealed EGO and its reduced form rEGO-based anodes. The battery performance of unannealed H_3BO_3 -EGO-based anode was also tested as displayed in Figure S5, the capacity of which was only 48.63 mAh g^{-1} at current density of 100 mA g^{-1} , because the residual intercalated tetraborate anions in H_3BO_3 -EGO may block the Na ion transport paths.

CONCLUSION

To improve the SIB anode performance for NG-derived EGO, we have optimized the sulfuric acid concentration for the packed bed electrochemical

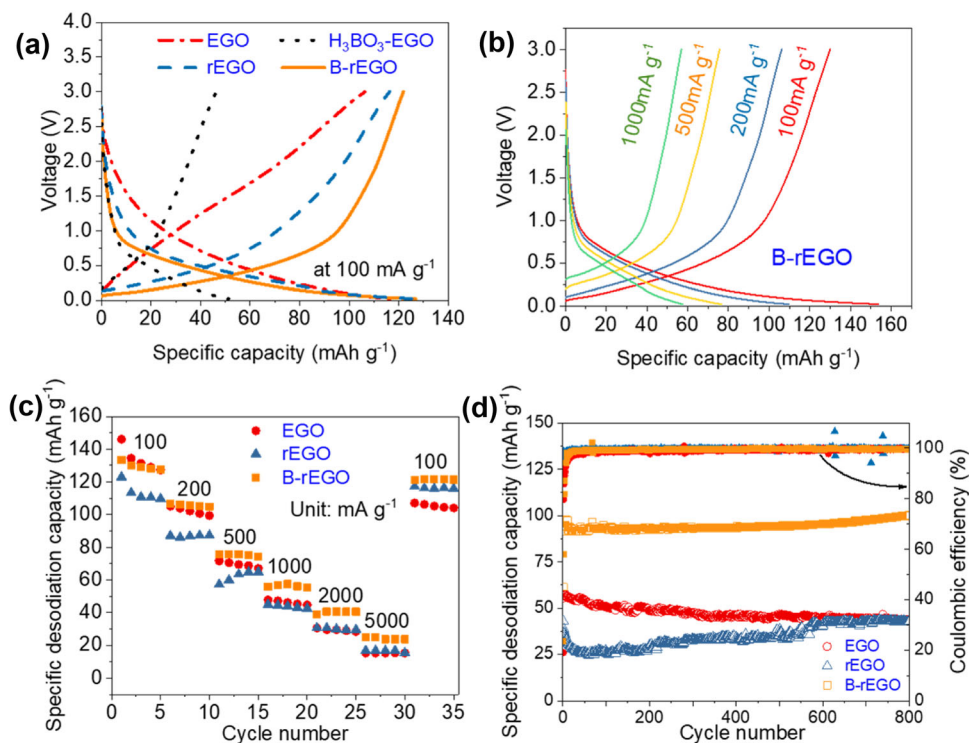


Fig. 6. Battery performance characterizations. (a) Galvanostatic charge/discharge curves of EGO, $\text{H}_3\text{BO}_3\text{-EGO}$, rEGO and B-rEGO based anodes at the current density of 100 mA g^{-1} . (b) Galvanostatic charge/discharge curves of B-rEGO anode at various current densities (data shown for the second cycle at each rate). Comparison of (c) rate performances and (d) long-term cycling performance at the current density of 500 mA g^{-1} of the EGO and highly reduced product (rEGO and B-rEGO)-based anode.

reaction. The chemical and physical properties of 7 M, 12 M and 16 M sulfuric acid-reacted EGO were characterized in detail, respectively. Saturated boric acid was added into 12 M sulfuric acid electrolyte to provide tetraborate anion to intercalate graphite for boron doping. High-temperature thermo-reduction was performed on the tetraborate anion intercalated EGO to fabricate highly reduced EGO (B-rEGO) of 0.21 at.% boron doped. The B doping can pronouncedly boost the sodium ion battery performance of EGO, contributing to high capacity of $129.59 \text{ mAh g}^{-1}$ at 100 mA g^{-1} and improved long-term cyclic stability under high current density of 500 mA g^{-1} (100.20 mA g^{-1} was attained after 800 cycles). This work offers a feasible and effective method to prepare low-cost, high-performance SIB electrodes from abundant, cheap graphite.

ACKNOWLEDGEMENTS

This work was financially supported by the Australian Research Council (DP190100120, FT200100015 and LP160101521).

CONFLICT OF INTEREST

The authors declare that they have no conflict of interest.

SUPPLEMENTARY INFORMATION

The online version contains supplementary material available at <https://doi.org/10.1007/s11837-021-04750-7>.

REFERENCES

1. R. Bi, C. Zeng, T. Ma, A. Etogo, X. Wang, and L. Zhang, *Electrochim. Acta* 284, 287. (2018).
2. Q. Liu, Z. Hu, M. Chen, Q. Gu, Y. Dou, Z. Sun, S. Chou, and S.X. Dou, *ACS Appl. Mater. Interfaces* 9, 3644. (2017).
3. J. Cao, Z. Sun, J. Li, Y. Zhu, Z. Yuan, Y. Zhang, D. Li, L. Wang, and W. Han, *ACS Nano* 15, 3423. (2021).
4. W. Sun, X. Rui, D. Zhang, Y. Jiang, Z. Sun, H. Liu, and S. Dou, *J. Power Sources* 309, 135. (2016).
5. J. Sun, H.-W. Lee, M. Pasta, H. Yuan, G. Zheng, Y. Sun, Y. Li, and Y. Cui, *Nat. Nanotechnol.* 10, 980. (2015).
6. Y.M. Chang, H.W. Lin, L.J. Li, and H.Y. Chen, *Mater. Today Adv.* 6, 100054. (2020).
7. A. Hashimoto, K. Suenaga, A. Gloter, K. Urita, and S. Iijima, *Nature* 430, 870. (2004).
8. S.E. Lowe, G. Shi, Y. Zhang, J. Qin, S. Wang, A. Uijtendaal, J. Sun, L. Jiang, S. Jiang, D. Qi, M. Al-Mamun, P. Liu, Y.L. Zhong, and H. Zhao, *ACS Appl. Nano Mater.* 2, 867. (2019).
9. J. Qin, Y. Zhang, S.E. Lowe, L. Jiang, H.Y. Ling, G. Shi, P. Liu, S. Zhang, Y.L. Zhong, and H. Zhao, *J. Mater. Chem. A* 7, 9646. (2019).
10. Y. Zhang, G. Shi, J. Qin, S.E. Lowe, S. Zhang, H. Zhao, and Y.L. Zhong, *ACS Appl. Electron. Mater.* 1, 1718. (2019).
11. J. Zhu, D. Yang, Z. Yin, Q. Yan, and H. Zhang, *Small* 10, 3480. (2014).

12. Y. Zhu, T. Wan, P. Guan, Y. Wang, T. Wu, Z. Han, G. Tang, and D. Chu, *J. Colloid Interface Sci.* 566, 375. (2020).
13. Y. Huang, R. Yu, G. Mao, W. Yu, Z. Ding, Y. Cao, J. Zheng, D. Chu, and H. Tong, *J. Alloys Compd.* 841, 155670. (2020).
14. A. Ramos, I. Cameán, N. Cuesta, and A.B. García, *Electrochim. Acta* 178, 392. (2015).
15. T.H. Nguyen, D. Yang, B. Zhu, H. Lin, T. Ma, and B. Jia, *J. Mater. Chem. A* 9, 7366. (2021).
16. T. Liao, C. Sun, A. Du, Z. Sun, D. Hulicova-Jurcakova, and S. Smith, *J. Mater. Chem.* 22, 8321. (2012).
17. Y. Wen, K. He, Y. Zhu, F. Han, Y. Xu, I. Matsuda, Y. Ishii, J. Cumings, and C. Wang, *Nat. Commun.* 5, 4033. (2014).
18. Y. Zhang, J. Qin, S.E. Lowe, W. Li, Y. Zhu, M. Al-Mamun, M. Batmunkh, D. Qi, S. Zhang, and Y.L. Zhong, *Carbon* 177, 71. (2021).
19. H. Zhang, D. Yang, A. Lau, T. Ma, H. Lin, and B. Jia, *Small* 17, 2007311. (2021).
20. J. Wan, F. Shen, W. Luo, L. Zhou, J. Dai, X. Han, W. Bao, Y. Xu, J. Panagiotopoulos, X. Fan, D. Urban, A. Nie, R. Shahbazian-Yassar, and L. Hu, *Chem. Mater.* 28, 6528. (2016).
21. N.P. Diklić, A.S. Dobrota, I.A. Pašti, S.V. Mentus, B. Johansson, and N.V. Skorodumova, *Electrochim. Acta* 297, 523. (2019).
22. P.V. Kumar, N.M. Bardhan, S. Tongay, J. Wu, A.M. Belcher, and J.C. Grossman, *Nat. Chem.* 6, 151. (2014).
23. Y.-J. Kang, S.C. Jung, J.W. Choi, and Y.-K. Han, *Chem. Mater.* 27, 5402. (2015).
24. Z. Liang, X. Fan, W. Zheng, and D.J. Singh, *ACS Appl. Mater. Interfaces* 9, 17076. (2017).
25. M. Cattelan, S. Agnoli, M. Favaro, D. Garoli, F. Romanato, M. Meneghetti, A. Barinov, P. Dudin, and G. Granozzi, *Chem. Mater.* 25, 1490. (2013).
26. Y.-B. Tang, L.-C. Yin, Y. Yang, X.-H. Bo, Y.-L. Cao, H.-E. Wang, W.-J. Zhang, I. Bello, S.-T. Lee, H.-M. Cheng, and C.-S. Lee, *ACS Nano* 6, 1970. (2012).
27. H. Wang, T. Maiyalagan, and X. Wang, *ACS Catal.* 2, 781. (2012).
28. D.-Y. Yeom, W. Jeon, N.D.K. Tu, S.Y. Yeo, S.-S. Lee, B.J. Sung, H. Chang, J.A. Lim, and H. Kim, *Sci. Rep.* 5, 9817. (2015).
29. M. Sahoo, K.P. Sreena, B.P. Vinayan, and S. Ramaprabhu, *Mater. Res. Bull.* 61, 383. (2015).
30. Z.-S. Wu, W. Ren, L. Xu, F. Li, and H.-M. Cheng, *ACS Nano* 5, 5463. (2011).
31. J. Gaidukevič, R. Pauliukaitė, G. Niaura, I. Matulaitienė, O. Opuchovič, A. Radzevič, G. Astromskas, V. Bukauskas, and J. Barkauskas, *Nanomaterials (Basel, Switzerland)* 8, 889. (2018).
32. H. Liu, H. Wang, and X. Zhang, *Adv. Mater.* 27, 249. (2015).
33. K. Erickson, R. Erni, Z. Lee, N. Alem, W. Gannett, and A. Zettl, *Adv. Mater.* 22, 4467. (2010).
34. Y.-X. Wang, S.-L. Chou, H.-K. Liu, and S.-X. Dou, *Carbon* 57, 202. (2013).
35. N.A. Kumar, R.R. Gaddam, S.R. Varanasi, D. Yang, S.K. Bhatia, and X.S. Zhao, *Electrochim. Acta* 214, 319. (2016).
36. S.E. Lowe, G. Shi, Y. Zhang, J. Qin, L. Jiang, S. Jiang, M. Al-Mamun, P. Liu, Y.L. Zhong, and H. Zhao, *Nano Mater. Sci.* 1, 215. (2019).
37. F. Liu, C. Wang, X. Sui, M.A. Riaz, M. Xu, L. Wei, and Y. Chen, *Carbon Energy* 1, 173. (2019).
38. Y. Sun, C. Du, M. An, L. Du, Q. Tan, C. Liu, Y. Gao, and G. Yin, *J. Power Sources* 300, 245. (2015).
39. M.I. Saidaminov, N.V. Maksimova, and V.V. Avdeev, *J. Mater. Res.* 27, 1054. (2012).
40. S. Pei, Q. Wei, K. Huang, H.-M. Cheng, and W. Ren, *Nat. Commun.* 9, 145. (2018).
41. S. Maass, F. Finsterwalder, G. Frank, R. Hartmann, and C. Merten, *J. Power Sources* 176, 444. (2008).
42. Y. Yang, and Z.G. Lin, *J. Appl. Electrochem.* 25, 259. (1995).
43. A.C. Ferrari, J.C. Meyer, V. Scardaci, C. Casiraghi, M. Lazzeri, F. Mauri, S. Piscanec, D. Jiang, K.S. Novoselov, S. Roth, and A.K. Geim, *Phys. Rev. Lett.* 97, 187401. (2006).
44. S. Claramunt, A. Varea, D. López-Díaz, M.M. Velázquez, A. Cornet, and A. Cirera, *J. Phys. Chem. C* 119, 10123. (2015).
45. A.C. Ferrari, S.E. Rodil, and J. Robertson, *Phys. Rev. B Condens. Matter* 67, 155306. (2003).
46. L.G. Cançado, A. Jorio, E.H.M. Ferreira, F. Stavale, C.A. Achete, R.B. Capaz, M.V.O. Moutinho, A. Lombardo, T.S. Kulmala, and A.C. Ferrari, *Nano Lett.* 11, 3190. (2011).
47. A.C. Ferrari, and D.M. Basko, *Nat. Nanotechnol.* 8, 235. (2013).
48. S. Eigler, C. Dotzer, and A. Hirsch, *Carbon* 50, 3666. (2012).
49. A.C. Ferrari, and J. Robertson, *Phys. Rev. B Condens. Matter* 61, 14095. (2000).
50. A. Sadezky, H. Muckenhuber, H. Grothe, R. Niessner, and U. Pöschl, *Carbon* 43, 1731. (2005).
51. S. Vollebregt, R. Ishihara, F.D. Tichelaar, Y. Hou, and C.I.M. Beenakker, *Carbon* 50, 3542. (2012).
52. T. Jawhari, A. Roid, and J. Casado, *Carbon* 33, 1561. (1995).
53. A. Dimiev, D.V. Kosynkin, L.B. Alemany, P. Chaguine, and J.M. Tour, *J. Am. Chem. Soc.* 134, 2815. (2012).
54. H. Zhao, J. Ye, W. Song, D. Zhao, M. Kang, H. Shen, Z. Li, and A.C.S. Appl. Mater. Interfaces 12, 6991. (2020).
55. X.-F. Luo, C.-H. Yang, and J.-K. Chang, *J. Mater. Chem. A* 3, 17282. (2015).
56. C. Bommier, T.W. Surta, M. Dolgos, and X. Ji, *Nano Lett.* 15, 5888. (2015).
57. Z.-J. Fan, W. Kai, J. Yan, T. Wei, L.-J. Zhi, J. Feng, Y.-M. Ren, L.-P. Song, and F. Wei, *ACS Nano* 5, 191. (2011).
58. Y. Wang, C. Wang, Y. Wang, H. Liu, Z. Huang, and A.C.S. Appl. Mater. Interfaces 8, 18860. (2016).
59. Z. Lin, Y. Yao, Z. Li, Y. Liu, Z. Li, and C.-P. Wong, *J. Phys. Chem. C* 114, 14819. (2010).
60. T. Kuila, S. Bose, P. Khanra, A.K. Mishra, N.H. Kim, and J.H. Lee, *Carbon* 50, 914. (2012).
61. J. Zhang, H. Yang, G. Shen, P. Cheng, J. Zhang, and S. Guo, *Chem. Commun.* 46, 1112. (2010).
62. Z. Tian, P. Yu, S.E. Lowe, A.G. Pandolfo, T.R. Gengenbach, K.M. Nairn, J. Song, X. Wang, Y.L. Zhong, and D. Li, *Carbon* 112, 185. (2017).
63. P. Yu, Z. Tian, S.E. Lowe, J. Song, Z. Ma, X. Wang, Z.J. Han, Q. Bao, G.P. Simon, D. Li, and Y.L. Zhong, *Chem. Mater.* 28, 8429. (2016).
64. N.R. Wilson, P.A. Pandey, R. Beanland, R.J. Young, I.A. Kinloch, L. Gong, Z. Liu, K. Suenaga, J.P. Rourke, S.J. York, and J. Sloan, *ACS Nano* 3, 2547. (2009).
65. R. Larciprete, S. Fabris, T. Sun, P. Lacovig, A. Baraldi, and S. Lizzit, *J. Am. Chem. Soc.* 133, 17315. (2011).
66. K. Krishnamoorthy, M. Veerapandian, K. Yun, and S.J. Kim, *Carbon* 53, 38. (2013).